Phase-controlled non-Markovian hysteresis in a nonlinear, non-Hermitian silicon microresonator

Stefano Biasi,[*,†] Stefano Gretter,[*] Bülent Aslan, Davide Olivieri, Riccardo Franchi,[‡] and Lorenzo Pavesi
Nanoscience Laboratory, Department of Physics, University of Trento, 38123 Trento, Italy

(Received 28 October 2025; revised 22 December 2025; accepted 12 January 2026; published 12 February 2026)

Non-Hermitian photonic systems, where gain, loss, and nonlinear interactions interplay, offer a fertile ground for realizing complex dynamical behavior such as broken reciprocity, self-oscillations, and excitable dynamics. Here, we report experimental observations of phase-controlled hysteresis in a nonlinear, non-Hermitian silicon microring resonator with dynamically tunable coupling between counterpropagating modes. By integrating independent thermal phase shifters, we modulate the intermodal feedback phase in real time and access regimes with different energy stored in the cavity, allowing us to investigate conditions governed by thermo-optic and free-carrier nonlinearities. We observe non-Markovian memory effects in the form of path-dependent phase trajectories: forward and reverse phase sweeps lead to distinct steady or oscillatory states, despite identical boundary conditions. This hysteresis is underpinned by a nonlocal bifurcation, where the system transitions from a stable fixed point to a saddle-node annihilation, to finally ending in a distant limit cycle. Our results demonstrate coherent phase control as a tool for accessing previously unseen bifurcation structures in photonics, and they establish a scalable platform for exploring neuromorphic dynamics beyond classical excitability.

DOI: 10.1103/fcsp-jw79

I. INTRODUCTION

Understanding the dynamics of non-Hermitian and nonlinear systems is a central challenge in contemporary physics with far-reaching implications for optics [1, 2], condensed matter [3], and complex systems science [4]. Unlike their Hermitian counterparts, non-Hermitian systems explicitly incorporate gain and loss, enabling a host of intriguing phenomena—many rooted in the presence of exceptional-point degeneracies [5,6]. These include unidirectional transport [7,8], mode chirality [9–11], coherent perfect absorption [12,13], and ultrasensitive sensing [14]. When non-Hermitian dynamics are combined with optical nonlinearities, the resulting systems support even richer behavior—including nonreciprocal transmission [15], mode-selective lasing [16], self-oscillation, and chaotic dynamics [17]. Beyond their fundamental interest, such systems offer an attractive framework for emulating the temporal complexity observed in biological excitable systems, such as neurons and cardiac tissue [18,19]. While traditional neuron models such as the Hodgkin-Huxley formalism [20] remain rooted in electrophysiological detail, photonic platforms provide minimal models that can exhibit multistability, threshold dynamics, and temporal memory—all essential features of neural processing [19,21]. This makes non-Hermitian photonic systems compelling for neuromorphic applications ranging from hardware-accelerated computing to adaptive signal processing [22,23].

Among the many nonlinear transitions found in such systems, Hopf bifurcations represent a ubiquitous route to self-sustained oscillations. They appear in systems ranging from chemical reactions (e.g., Belousov-Zhabotinsky oscillators [24]) to neurodynamics and laser physics [18]. In minimal two-level system models, a Hopf bifurcation arises when a pair of complex-conjugate eigenvalues crosses the imaginary axis as a control parameter—typically the coupling strength or feedback gain—is varied. Below threshold, the system relaxes to a fixed point; above threshold, this point becomes unstable and gives way to a limit cycle, whose amplitude typically scales as the square root of the control parameter's excess [25]; however, the dynamics can be profoundly

[*]These authors contributed equally.
[†]Contact author: stefano.biasi@unitn.it
[‡]Present address: Nanomaterials and Nanostructure Optics, Department of Electrical and Computer Engineering, Boston University, Boston, Massachusetts 02215, USA.

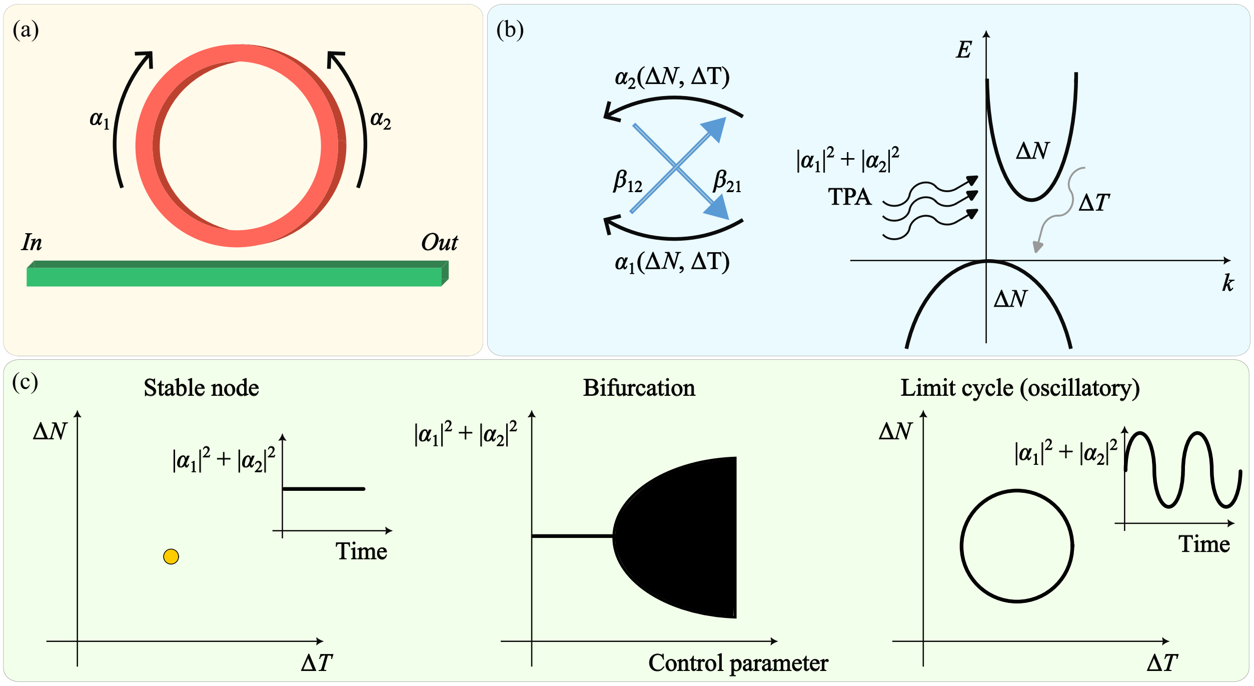

FIG. 1. Hopf bifurcation and (memory-induced) dynamics in a nonlinear two-level photonic system. (a) Schematic of a nonlinear microring resonator (red) supporting two counterpropagating modes, α_1 and α_2, coupled to a bus waveguide (green). The system is driven through an input port (*In*) and monitored at the output port (*Out*). (b) Energy-level representation of the coupled-mode dynamics in the microring. The intermodal coupling coefficients β_{12} and β_{21} govern the cavity stored energy $|\alpha_1|^2 + |\alpha_2|^2$. Two-photon absorption of the propagating cavity modes generates free carriers (ΔN). This is represented in an energy-momentum diagram on the right, which represents the indirect silicon semiconductor. The free carriers relax, increasing the effective temperature (ΔT) of the cavity. Both ΔN and ΔT feed back into the system, modulating the cavity modes. (c) Dynamical signatures of a Hopf bifurcation in the cavity energy (central plot). As a control parameter increases, the system transitions from a stable fixed point (left) to a limit cycle (right). Bifurcation diagrams and time traces of $|\alpha_1|^2 + |\alpha_2|^2$ reveal the onset of self-sustained oscillations. Memory effects—such as delayed feedback or non-Markovian dissipation—shift the bifurcation threshold and stabilize coherent oscillatory states.

modified when memory effects are introduced—either via delayed feedback, non-Markovian dissipation, or history-dependent couplings. These forms of effective time nonlocality cause the system's present state to depend explicitly on its past trajectory, shifting bifurcation thresholds, modifying stability, or enabling oscillations that are otherwise forbidden [26,27]. In photonic systems, such memory is intrinsic: finite photon lifetimes, thermal feedback, carrier dynamics, and cavity-mediated interactions all provide natural reservoirs of memory. Far from being a perturbation, memory here acts as a functional resource, supporting complex temporal behavior in architectures of minimal physical complexity [28,29]. In this work, the term "non-Markovian" is used in the context of effective optical-field dynamics, where the system's evolution depends on its history as a result of nonlinear light-matter interactions, rather than in the conventional open-quantum-system sense [30]. The silicon-on-insulator photonics platform is particularly well suited to exploring this interplay between nonlinearity, non-Hermiticity, and memory. It offers low-loss waveguides, strong Kerr and two-photon absorption (TPA) nonlinearities, and full integration with complementary metal-oxide-semiconductor (CMOS)-compatible control electronics [31,32]. In silicon microresonators, TPA generates free carriers whose relaxation leads to localized heating and refractive-index shifts, creating rich carrier-thermal feedback loops [31,33]. Combined with directional coupling and controlled dissipation, these effects have enabled the observation of nonreciprocity [34,35], chiral symmetry breaking [36,37], and even excitable dynamics [21]. The convergence of non-Hermitian physics, nonlinear optics, and neuromorphic photonics is opening previously inaccessible frontiers in the design and control of light in complex systems.

Here, we investigate a non-Hermitian, nonlinear photonic system based on a passive silicon microring resonator with tunable coupling between counterpropagating optical modes. This system—the dynamically reconfigurable unified microresonator (DRUM)—exploits feedback loops where phase shifters (PSs) and Mach-Zehnder interferometers (MZs) control the coupling between counterpropagating modes to modulate the directionality and strength of intermodal energy exchange. Through this architecture, we study how intrinsic feedback mechanisms and non-Markovian effects give rise to memory, multistability, and self-sustained oscillations. The physical mechanisms at play are illustrated in Fig. 1. Figure 1(a) shows a microring resonator, which supports two propagating modes (α_1 and α_2), with the bus waveguide. The input signal is coupled to the *In* port while the output signal is measured from the *Out* port. Figure 1(b) represents the effective two-level dynamical system, which models the microring resonator. This minimal model highlights the tunable intermodal coupling coefficients (β_{12} and β_{21}) that control the system's nonlinear dynamics. Nonlinear dynamics are governed by TPA-generated free carriers (ΔN), which relax and produce localized temperature increases (ΔT), thereby shifting the effective resonance. The optical energy within the microring ($|\alpha_1|^2 + |\alpha_2|^2$)—modulated by these carrier and thermal dynamics—feeds back into the system, establishing a non-Markovian response characterized by memory effects. The non-Markovian response arises from the dependence of a state on its prior dynamical evolution. This introduces history dependence, shaping the optical fields [$\alpha_1(\Delta N, \Delta T)$ and $\alpha_2(\Delta N, \Delta T)$] through fast free-carrier ($\propto$1 ns) and slow thermal ($\propto$100 ns) dynamics. Figure 1(c) shows the resulting bifurcation diagram, with transitions from steady states (stable node) to oscillatory states (limit cycle), driven by variations in the control parameter. Our results reveal how intrinsic optical memory and non-Hermitian coupling conspire to produce a wide range of dynamical regimes—including hysteresis, path dependence, and bifurcations. Together, these results establish DRUM as a versatile platform for probing non-Hermitian nonlinear photonic dynamics, with implications for neuromorphic photonics, excitability engineering, and optical computing.

II. THE NONLINEAR DYNAMICALLY RECONFIGURABLE UNIFIED MICRORESONATOR

We investigate aforementioned physics using a tunable resonator architecture: the DRUM, shown in Fig. 2(a). The system comprises a bus waveguide [green line in Fig. 2(a)] side-coupled to a microring resonator [red line in Fig. 2(a)], which is further coupled to two additional side waveguides [light-blue lines in Fig. 2(a)], referred to as side lobes. These side lobes enable controlled recirculation of propagating modes within the cavity in both the clockwise (α_1) and counterclockwise (α_2) directions. Each side lobe integrates a thermally tunable MZ and PS, actuated via microheaters. These elements allow for electrical control of the intermodal coupling between the counterpropagating modes [Fig. 1(b)]. Specifically, the PSs adjust the coupling phases (ϕ), while the MZs control the amplitudes ($|\beta|$) of the complex coupling coefficients, denoted as $\beta_{12} = |\beta_{12}|e^{\phi_{12}}$ and $\beta_{21} = |\beta_{21}|e^{\phi_{21}}$. The left-side lobe controls β_{12}, while the right-side lobe controls β_{21}, enabling the system to operate under either Hermitian or non-Hermitian coupling conditions [38]. The device is excited via a continuous-wave input light injected through the grating coupler labeled *In*, which directly excites the counterclockwise mode α_2. The right-hand side-lobe partially converts α_2 into α_1, and the left-hand side-lobe reciprocally converts α_1 back into α_2. As the energy is exchanged between the modes, the system evolves into a state in which both α_1 and α_2 circulate within the microring, governed by the direction-dependent coupling dynamics.

The dynamics of the DRUM is modeled using the temporal coupled-mode theory, which describes the evolution of the optical field amplitudes α_1 and α_2 as

$$\begin{aligned}\frac{d\alpha_1}{dt} &= \left(i(\omega_\mathrm{r} - \omega) - \frac{\gamma_\mathrm{loss}}{2}\right)\alpha_1 - \beta_{21}\alpha_2,\\ \frac{d\alpha_2}{dt} &= \left(i(\omega_\mathrm{r} - \omega) - \frac{\gamma_\mathrm{loss}}{2}\right)\alpha_2 - \beta_{12}\alpha_1 + i\sqrt{\gamma_\mathrm{coup}}E_\mathrm{in},\end{aligned} \tag{1}$$

where $\omega_r = \omega_r^0 + \delta\omega_N \Delta N + \delta\omega_T \Delta T$ is the power-dependent resonant frequency of the microring, γ_loss is the power-dependent total loss rate, which includes both the intrinsic and extrinsic losses, and E_in is the input field (for more details, see the Supplemental Material [39]). These optical dynamics are coupled to the evolution of the free-carrier population (ΔN) and the local temperature shift (ΔT), governed by [40]

$$\begin{aligned}\frac{d\Delta N}{dt} &= -\frac{\Delta N}{\tau_\mathrm{fc}} + N_{a4}(|\alpha_1|^2 + |\alpha_2|^2)^2\\ \frac{d\Delta T}{dt} &= -\frac{\Delta T}{\tau_\mathrm{th}} + T_{a2}(|\alpha_1|^2 + |\alpha_2|^2),\end{aligned} \tag{2}$$

where τ_fc and τ_th are the free-carrier and thermal relaxation times, respectively; N_{a4} is a constant, and T_{a2} is a function of the energy circulating inside the ring and the free carrier concentration whose value and definitions are given in Sec. S2 of the Supplemental Material [39]. Equations (1) and (2) highlight the nonlinear interplay between the optical fields and the carrier-thermal dynamics. This coupling introduces a non-Markovian character to the system: the evolution of the optical fields depends not only on the instantaneous field amplitudes but also on the history of the cavity energy. As a result, the system retains memory of its past states, a key feature in enabling complex dynamical behavior.

Full analytical solutions of Eq. (1), along with detailed definitions and derivations of the parameters in Eq. (2), are provided in Secs. S1 and S2 of the Supplemental Material [39], respectively; however, valuable insights can be gained by considering the stationary solutions to Eq. (1)

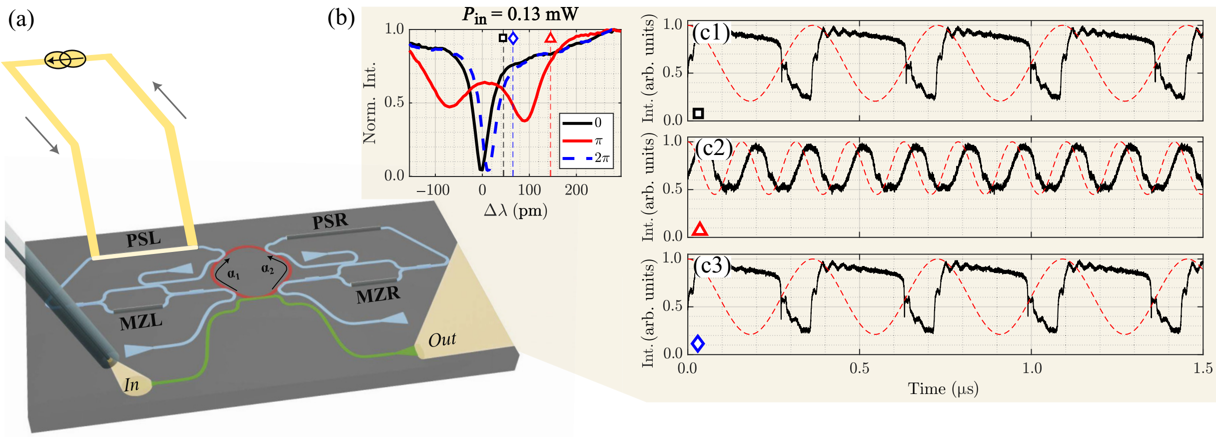

FIG. 2. Spectral and temporal response of the DRUM for a phase change. (a) DRUM photonic circuit: the green line represents the bus waveguide, the red line represents the microring resonator, and the blue lines represent the side lobes with integrated thermal heaters (gray lines), which are driven by injecting a current through metal wires (yellow line, shown for only one heater for simplicity). The thermal heaters are used to realize phase shifters (PSL, left; PSR, right) and Mach-Zehnder interferometers (MZL, left; MZR, right). Triangles are grating couplers. The input signal is provided by a stripped optical fiber coupled to the bus waveguide by a grating coupler at the *In* port. Applying a current to PSL tunes the phase ϕ_{12} of the intermodal coupling coefficients. (b) Low-power linear transmission spectra for $\phi_{12} = 0, \pi$, and 2π as a function of wavelength detuning $\Delta\lambda$, defined as the difference between the input laser wavelength and the cold microresonator's resonant wavelength at $\phi_{12} = 0$. The input power ($P_{\rm in}$) is 0.13 mW in the bus waveguide. (c1)–(c3) Time-dependent normalized transmission at high power ($P_{\rm in} = 21.1$ mW) for $\phi_{12} = 0, \pi$, and 2π. Each corresponds to the wavelength detunings highlighted in Fig. 2(b) by the black, blue dashed, and red lines associated with a square, diamond, and triangle marker, respectively. The black line represents the optical signal, while the red dashed line shows a sine curve at the fundamental self-pulsing frequency deduced by the Fourier transform of the time-dependent transmission.

in the linear regime (i.e., at low input powers where free-carrier and thermal effects are negligible) [38]. In this limit, the relationship between the intracavity energy ($|\alpha_1|^2 + |\alpha_2|^2$) and the intermodal coupling coefficients becomes analytically tractable. In this case,

$$\alpha_1 = \frac{\sqrt{\beta_{12}\beta_{21}}}{\beta_{12}} \frac{i\sqrt{\gamma_{\rm coup}}E_{\rm in}}{2} \left(\frac{1}{\lambda_2} - \frac{1}{\lambda_1}\right), \tag{3}$$

$$\alpha_2 = -\frac{i\sqrt{\gamma_{\rm coup}}E_{\rm in}}{2} \left(\frac{1}{\lambda_2} + \frac{1}{\lambda_1}\right), \tag{4}$$

where

$$\lambda_{1,2} = i\,(\omega_{\rm r} - \omega) - \frac{\gamma_{\rm loss}}{2} \mp \sqrt{\beta_{21}\beta_{12}}, \tag{5}$$

in which ω is the laser angular frequency and $\lambda_{1,2}$ are the eigenvalues of the Jacobian describing the DRUM.

III. RESULTS

Among the various control parameters available for exploring the nonlinear dynamics of the DRUM—such as input optical power, laser detuning from the cold-cavity resonance, or coupling-coefficient strength—we focus on the phase of the coupling coefficients. This choice is motivated by the fact that the phases ϕ_{12} and ϕ_{21} directly govern the coherent interaction between counterpropagating modes. Since Eqs. (3) and (4) depend on the complex product $\beta_{12}\beta_{21} = (|\beta_{12}||\beta_{21}|)e^{i(\phi_{12}+\phi_{21})}$, variations in the sum $(\phi_{12} + \phi_{21})$ can lead to significantly different intracavity energies $|\alpha_1|^2 + |\alpha_2|^2$ even for fixed coupling-coefficient amplitudes. We systematically investigate the DRUM's nonlinear response by tuning these phases via the integrated PSs. This tuning effectively controls the phase of the energy-exchange mechanism between counterpropagating modes, thereby allowing us to manipulate the system's nonlinear optical behavior. A particularly striking feature is the system's path-dependent memory: when the phase is swept along a closed loop differing by 2π, the final optical state depends sensitively on the direction of the sweep: *forward* (from 0 to 2π) and *reverse* (from 2π to 0) trajectories yield distinct stationary or quasistationary responses, despite ending at nominally identical phase points. This directional memory is a hallmark of non-Markovian dynamics and underpins the system's rich bifurcation structure.

In the following, we present and analyze the results in four subsections. First, we provide an overview of the DRUM by reporting its spectral and temporal optical response at the initial, intermediate, and final phase states. In the second subsection, we demonstrate how the temporal optical response evolves after a full forward and reverse cycle. We highlight the path dependence and demonstrate the presence of an optical bifurcation. In the third, we experimentally investigate saddle-node annihilation by measuring the onset time of the self-pulsing (SP) and identifying signatures of a saddle-node ghost. Finally, we show that simultaneous sweeping of both PSs—while keeping their sum ($\phi_{12} + \phi_{21}$) constant—preserves the initial SP state throughout the sweep.

A. Operating principle and optical signals at phase boundaries

The optical response of the DRUM is measured using the experimental setup described in Appendix A. The signal is collected at the output grating coupler of the bus waveguide (*Out*) [Fig. 2(a)]. At low optical power, i.e., in the linear regime, the spectral shape of the transmission intensity varies as a function of the currents applied to the MZs or PSs [38]. As shown in Fig. 2(b), varying the phase applied via PSL transforms the initial Lorentzian transmission profile (measured with no current applied, shown as black line) into a nearly balanced mode doublet at a phase of π (red line). In these measurements, the initial condition is defined by setting all MZs and PSs in the side lobes to zero current. Then, only PSL is actuated by applying a current I_{PSL}. The solutions of Eq. (1) indicate that the transmission spectrum depends on the phase sum $\phi_{12} + \phi_{21} = \phi_{12}^0 + \phi_{12}(I_{\mathrm{PSL}}) + \phi_{21}^0$, where the superscript 0 denotes the phase with no current applied, and $\phi_{12}(I_{\mathrm{PSL}})$ is the phase induced by the injected current. For simplicity, we consider the resonance that satisfies $\phi_{12}^0 + \phi_{21}^0 = 0$, so that changes in ϕ_{12} directly control the phase difference (see Sec. S1 of the Supplemental Material [39] for more details). The transformation in the spectral shape shown in Fig. 2(b) is driven by the changes in the intermodal coupling. At $\phi_{12} = 0$, the two eigenvalues are nearly split solely in their real parts [Eq. (5)], yielding a single Lorentzian peak. At $\phi_{12} = \pi$, the splitting of the eigenvalues is maximized in the imaginary part, leading to a spectral doublet. Crucially, this control over the coupling is achieved solely by tuning the phases of the intermodal coupling coefficients, without altering their amplitudes. After a full 2π phase cycle, the spectrum returns to its original Lorentzian shape (blue dashed line), confirming the periodicity of the phase-controlled coupling. While the Lorentzian profiles at $\phi_{12} = 0$ and 2π are spectrally identical in shape, the resonance at 2π exhibits a redshift of approximately 16 pm. This shift is attributed to thermal crosstalk affecting the microring, despite the presence of thermal-isolation trenches designed to mitigate such effects. This thermal shift does not impact our qualitative analysis but introduces a known offset in the spectral position of the resonance at $\phi_{12} = 2\pi$, which is accounted for in the nonlinear measurements. Further details on the DRUM's linear spectral response are available in Ref. [38].

At relatively high optical powers, nonlinear optical effects emerge in the DRUM due to light-matter interactions dominated by TPA [Fig. 1(b)]. TPA generates free carriers, leading to both free-carrier absorption and free-carrier dispersion [31,33]. These carriers alter the microresonator's refractive index through absorption-induced heating, which redshifts the resonance via the thermo-optic effect, and through plasma dispersion, which blueshifts it. Importantly, these effects scale differently with the cavity energy: the thermo-optic shift depends linearly on the intracavity intensity, whereas the carrier-induced index change scales quadratically [41]. Their interplay is further shaped by distinct relaxation timescales—tens of nanoseconds for carriers and hundreds for thermal dissipation [42,43]. Together, these mechanisms can give rise to self-sustained oscillations, or SP, wherein a continuous-wave input is converted into a periodic output signal [44,45]. As shown in Fig. 1(c), intermodal energy pushes the system from a stable fixed point to a limit cycle, marking the onset of nonlinear oscillatory dynamics.

Figures 2(c1)–2(c3) present the normalized transmission intensity over time for three different phase settings, $\phi_{12} = 0$, π, and 2π. These correspond to the wavelength detunings marked by the black, red, and blue dashed lines in Fig. 2(b), respectively. The measured signals are shown as solid black traces, while the red dashed lines indicate sine waves at the fundamental SP frequency, extracted from the Fourier spectra. For each measurement, the current is first applied to PSL, and the laser is turned on only after thermal equilibrium is reached. This protocol ensures that the observed DRUM state depends solely on the final value of ϕ_{12}, independent of the path taken to reach it. The SP waveform evolves significantly with phase, reflecting changes in the interaction between counterpropagating modes. This manipulation affects both signal shape and frequency, which spans from (2.75 ± 0.14) MHz to (6.35 ± 0.14) MHz, transitioning from a characteristic through-port waveform to one that is nearly sinusoidal [41]. Notably, at $\phi_{12} = 2\pi$, the DRUM response is nearly identical to that at $\phi_{12} = 0$, as seen by comparing Figs. 2(c1) and 2(c3). This periodicity in the SP regime mirrors the symmetry observed in the linear transmission response [Fig. 2(b)].

B. Hysteresis and memory with full-cycle forward and reverse phase sweep

In the linear regime, the steady state is determined solely by the sum of the final phase ($\phi_{12} + \phi_{21}$), regardless of the path taken to reach it. Neither the rate of change nor the signs of ϕ_{12} and ϕ_{21} affect the final steady-state response. This behavior is explicitly demonstrated in the analytical solution provided in Sec. S1 [Eq. (16)] of the Supplemental Material [39]. After all, the intermediate states encountered on the way to a given phase are not continuously connected; each transition occurs without reference to the prior state. We refer to this as a *no-memory* operation, and it is consistent with the results of Ref. [38]. More information about no-memory operation of DRUM is given in Sec. S3 of the Supplemental Material [39].

Unlike in the linear regime, the DRUM—while supporting no-memory operation—exhibits strong path dependence (hysteretic behavior) in the nonlinear regime, enabled by the coupled evolution of ΔN and ΔT inside the microresonator [Fig. 1(b)]. Both quantities are influenced by the optical field intensity stored in the cavity. As a result, when the phase controlling the energy exchange between counterpropagating modes varies slowly relative to the carrier and thermal-relaxation timescales, the system begins to exhibit *memory*. This memory results in a strong dependence of the system's final state on the trajectory taken through the parameter space.

Experimentally, this memory can be accessed by fixing the input laser power and wavelength—setting the DRUM to a known steady state—and varying only the currents applied to PSL. Figures 3(a) and 3(b), show maps of the measured SP frequency as a function of the intermodal coupling phase ϕ_{12} and the laser detuning $\Delta\lambda$, with an input power of approximately 21.1 mW in the bus waveguide. The SP frequency is extracted from the dominant component of the Fourier transform of the time-domain optical transmission and color-coded according to the scale shown at the top of the panels; white regions correspond to steady states without oscillations. Figure 3(a) shows the result of a full forward phase sweep from $\phi_{12} = 0$ to 2π, while Fig. 3(b) shows a full reverse sweep from 2π to 0. These continuous phase sweeps are performed while the DRUM is optically loaded, thus preserving memory of the previous intracavity state—an operation we refer to as *path-dependent phase rotation*. By contrast, between different laser detuning values, the system is reset to its rest state by turning off the input power and allowing it to thermally and electronically discharge. The forward and reverse ϕ_{12} sweeps are experimentally implemented by increasing or decreasing the applied current to the PSL, respectively. As shown in the study of the linear response of the DRUM [38], variation of ϕ_{12} induces a change in the quality factor of the structure, which varies from a maximum value of $Q = 3.1 \times 10^4$ at $\phi_{12} + \phi_{21} = 0$ to a minimum value of $Q = 8.9 \times 10^3$ at $\phi_{12} + \phi_{21} = \pi$. The input power used in the measurements presented here was kept constant at a value sufficient to promote SP states within the explored phase values and input-laser wavelength scanning ranges.

The initial states for both sweeps—$\phi_{12} = 0$ in the forward direction and $\phi_{12} = 2\pi$ in the reverse direction—show comparable behavior, consistent with the 2π periodicity of the intermodal phase and with earlier observations in Sec. III A; however, the two maps have different shapes, suggesting that a forward sweep leads to a different state evolution than a reverse one. This bistable behavior is particularly evident in the SP island formed in the lower part of both maps. For detunings greater than 60 pm, the system's evolution between the forward and reverse scans differs. In the forward direction, the system briefly enters a pulsing state but exits it as ϕ_{12} increases, returning to a nonoscillating regime. In contrast, the reverse sweep leads to persistent oscillations even as ϕ_{12} approaches zero. These distinct trajectories, starting from equivalent initial conditions, confirm the presence of optical bistability. Numerical simulations, as shown in Figs. 3(c) and 3(d), reproduce the main features of the experiment, including the presence and shape of the SP islands, as well as the different state trajectories for opposite sweep directions. Although the model does not account for thermal crosstalk between heaters, it faithfully captures the underlying nonlinear dynamics. The bistable behavior is also reflected in the normalized average transmission intensity, shown in Figs. 3(e) and 3(f) for forward and reverse sweeps, respectively. These intensities are averaged over approximately 7 μs and normalized to the peak value of all the sweeps. Differences in transmission levels at high detuning and low ϕ_{12} further highlight the presence of distinct final states. Simulated maps in Figs. 3(g) and 3(h) again match experimental trends well.

To better evidence the observed bistability, we extract cross sections of the maps at the detuning indicated by the black dashed line in Fig. 3. Figures 4(a) and 4(b) show the evolution of the measured SP frequency and normalized average transmission as a function of ϕ_{12} for both sweep directions. The forward sweep (black) exhibits a threshold near $\phi_{12} \sim \pi/2$, above which oscillations emerge. Below this threshold, the system remains in a steady, nonpulsing state with high transmission. In contrast, the reverse sweep (red) retains SP even at $\phi_{12} = 0$, with a corresponding drop in average transmission. These contrasting final states highlight a clear hysteresis loop in both observables. Theoretical simulations, as shown in Figs. 4(c) and 4(d), reproduce the experimental trends, validating the underlying model and enabling a detailed investigation of the equilibrium structure and its evolution with the control parameter.

Figures 4(e)–4(g) show the refined nullclines, where $|\alpha_1|^2$ is plotted against $|\alpha_2|^2$ for $\phi_{12} = 0, 0.37\pi$, and 0.75π, corresponding to phase points I, II, and III in Fig. 4(c). As detailed in Sec. S4 of the Supplemental Material [39], intersections of these nullclines identify equilibrium points of the system. During a phase scan, the DRUM evolves toward different equilibria, indicated by numbered markers. Those that govern the system's dynamics during the path-dependent phase rotation are highlighted in yellow for forward scans and in green for reverse scans, respectively.

The plot in Fig. 4(e), corresponding to $\phi_{12} = 0$ [marked as I in Fig. 4(c)], shows three intersections of the refined nullclines, denoted as points #1, #3, and #6. At this phase, the system is at the starting point of a forward phase scan—when the cavity is initially unloaded—and

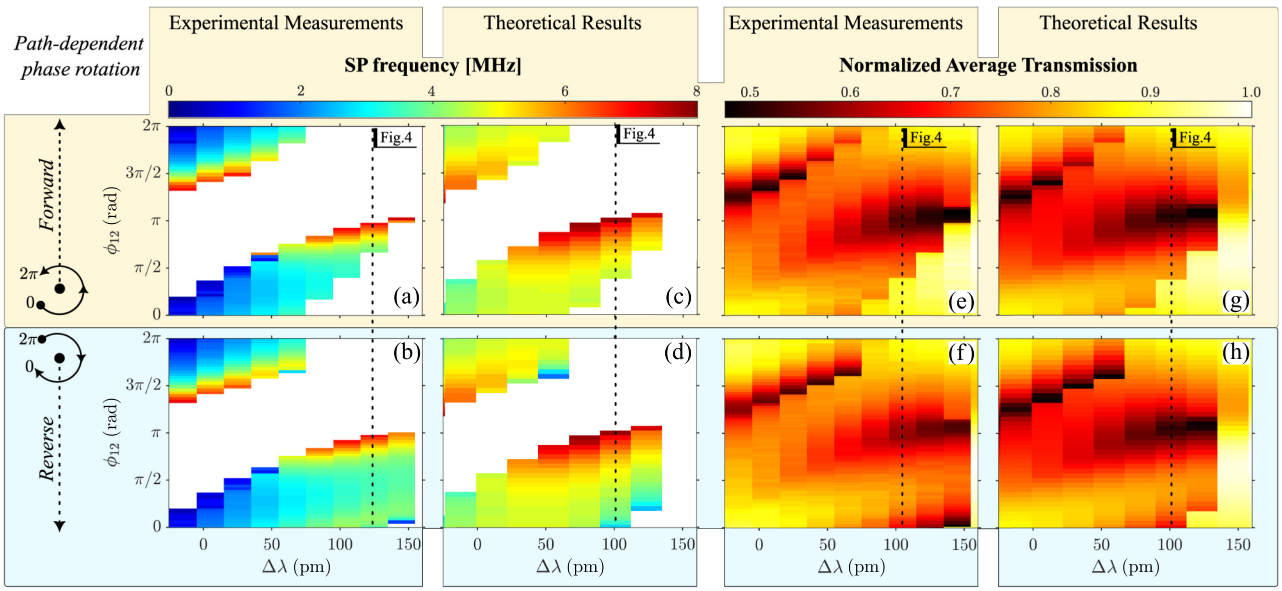

FIG. 3. Maps of the SP frequency and the normalized average transmission under full-cycle path-dependent phase rotation. (a),(b) and (c),(d) experimental and simulated SP frequency as a function of wavelength detuning ($\Delta\lambda$) and ϕ_{12}. (e),(f) and (g),(h) experimental and simulated normalized average transmission versus ϕ_{12} and $\Delta\lambda$. The top row [(a),(c),(e),(g)] shows a full-cycle *forward* phase sweep from $\phi_{12} = 0$ to 2π; the bottom row [(b),(d),(f),(h)] shows a *reverse* sweep from $\phi_{12} = 2\pi$ to 0. In both cases, this is conducted without resetting the initial state between steps, i.e., they are *path-dependent phase rotations*. The black dashed lines mark the $\Delta\lambda$ values of the results shown in Fig. 4. The color codes are shown on top of each map.

at the end of a reverse phase scan—when the cavity is still energetically charged. Consequently, during a forward scan, the total intracavity energy ($|\alpha_1|^2 + |\alpha_2|^2$) is low, and the system relaxes toward the lowest-energy equilibrium point, #1 (highlighted in yellow). Conversely, in the reverse scan, the cavity energy remains high, and the system approaches the highest-energy equilibrium point, #6 (green). A linear stability analysis via eigenvalue evaluation (see Sec. S5 of the Supplemental Material [39]) classifies point #1 as a stable node, point #3 as a saddle node, and point #6 as an unstable node. As the phase is increased to $\phi_{12} = 0.37\pi$ in a forward scan [line II in Fig. 4(c)], the attractive node #1 and the saddle node #3 coalesce and annihilate in a standard *saddle-node annihilation* [46]. This leads to a configuration with three equilibrium points, #5 (unstable), #2$^+$ (saddle), and #2$^-$ (stable), shown in Fig. 4(f), as #2 for the annihilation site. Upon further increasing ϕ_{12} to 0.75π [line III in Fig. 4(c)], the nullclines separate at the location of the former saddle-node bifurcation, leaving a single intersection at point #4 [Fig. 4(g)]. This point is unstable and gives rise to SP behavior. In a reverse phase scan, the system initially occupies an SP state associated with the high-energy point #4. As the phase is decreased, it tracks the sequence of high-energy, unstable equilibrium points #4, #5, and #6 (green), thereby sustaining the SP dynamics. Consequently, at $\phi_{12} = 0$ (line I), whether the system exhibits SP or not depends on both the initial condition and the direction of the phase scan. This demonstrates the path-dependent nature of the DRUM's nonlinear dynamics.

Figure 4(h) illustrates the system's evolution during a forward phase scan in a phase portrait representation, where the variation in ΔN is plotted against the corresponding variation ΔT. This plot combines multiple phase spaces evaluated at different values of ϕ_{12}, effectively capturing the system's dynamical landscape. Equilibrium points are marked with different symbols—triangles for $\phi_{12} = 0$, squares for 0.37π, and circles for 0.75π—with matching marker shapes indicating coexistence at a given phase. The numerical labels correspond to the equilibrium points previously shown in Figs. 4(e)–4(g).

At the beginning of the scan, $\Delta N = \Delta T = 0$, as the cavity is initially unloaded. Once the input laser is switched on, the internal cavity energy increases, triggering the generation of free carriers and a rise in temperature. The system is then drawn toward the stable node #1. As ϕ_{12} increases (from state I to II), equilibrium points #1 and #3 move toward each other (black dashed arrows), but the system remains attracted to #1 throughout this stage. When the saddle-node bifurcation occurs—where points #1 and #3 annihilate into point #2—the system loses its stable fixed point and transitions to the basin of attraction around the unstable equilibrium #5 (the transition is indicated by the blue dashed line). This transition is experimentally identified by the evolution of the dynamic from a steady state to an oscillatory regime. Upon further increasing ϕ_{12} to

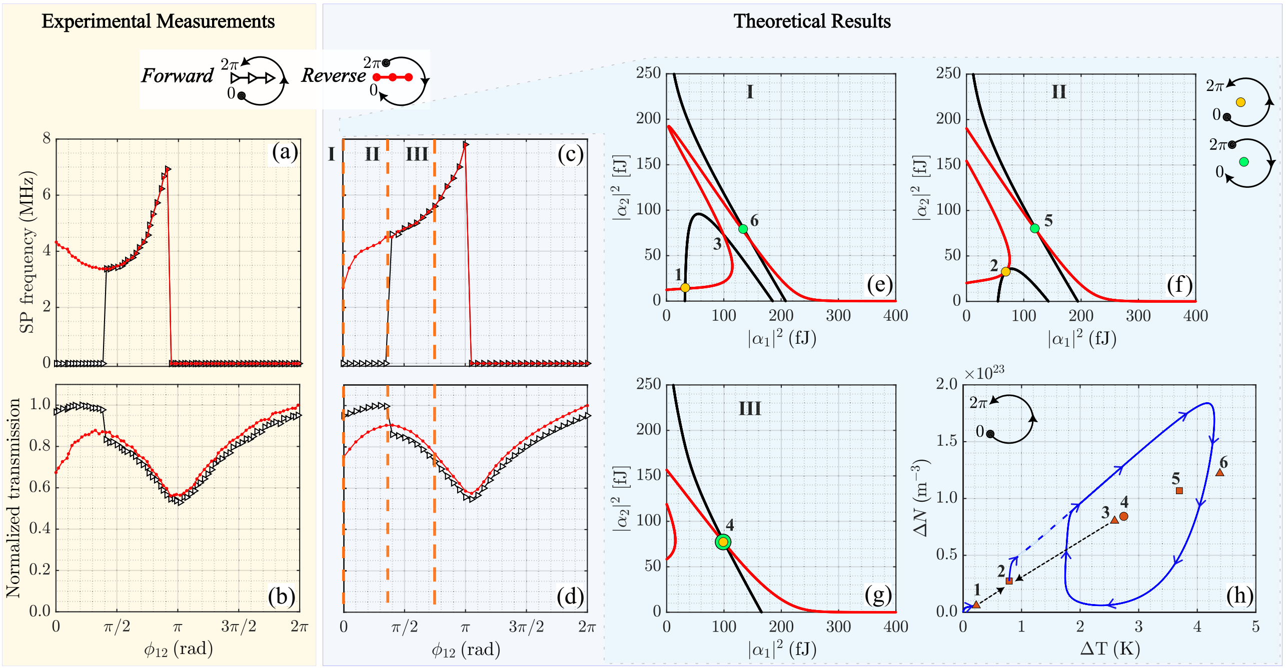

FIG. 4. Optical bifurcation under full-cycle path-dependent phase rotation. (a),(b) Experimental results for the self-pulsing (SP) frequency and normalized average transmission as a function of ϕ_{12}, during a full sweep from $\phi_{12} = 0$ to 2π (*forward*, black lines and triangles) and from $\phi_{12} = 2\pi$ to 0 (*reverse*, red lines and dots). These data refer to a fixed-wavelength detuning, indicated by the black dashed lines in Fig. 3. (c),(d) Simulation results. The vertical dashed lines refer to the phases where further analysis has been performed. (e)–(g) Refined nullclines for ϕ_{12} values denoted by Roman numerals in (c) ($\phi_{12} = 0$, 0.37π, and 0.75π). Yellow (green) points represent the equilibrium states reached by sweeping ϕ_{12} from 0 to 2π (or from $\phi_{12} = 2\pi$ to 0). Each equilibrium point is labeled with a different number. (h) Phase-space trajectories during the *forward* sweep ($\phi_{12} = 0$ to 2π). The system evolves through a saddle-node annihilation. Symbols and numbers refer to the equilibrium points in (e) triangles, (f) squares, and (g) circles. The black dashed line shows the system evolution from I to II, while the blue dashed line shows the system evolution from II to III. The blue line shows the system oscillation in a limit cycle in III.

0.75π (III), the system begins to orbit around the unstable equilibrium point, following the trajectory shown by the solid blue line. This closed-loop trajectory is a hallmark of SP behavior in the phase space. In the case of a reverse phase sweep, the system enters an SP regime by orbiting around point #4, starting from a loaded cavity. As ϕ_{12} decreases, the encircling behavior shifts progressively toward the upper-right quadrant of the ΔN-ΔT plane. During this evolution, the system successively encircles points #5 and #6, which lie near the center of the orbit. The trajectory clearly shows that at $\phi_{12} = 0$, in the reverse sweep, the system remains in an SP state. This analysis confirms that the presence or absence of SP at a given phase value depends not only on the actual system parameters but also on the history of energy evolution within the cavity, underscoring the intrinsic path dependence of the nonlinear DRUM dynamics.

At this stage, it is worth emphasizing the distinctive nature of the bifurcation mechanism underlying the observed dynamics, as revealed through both experimental results and theoretical modeling. The system is initially trapped into a stable node in the presence of a saddle node and a distant limit cycle. The saddle-node annihilation triggers the system to a transition toward a new attractor. During this transition, the system evolves toward a preexisting distant limit cycle that does not pass through the saddle-node annihilation point. Such a transition gives birth to a breakage of the continuous time-translation symmetry and a pronounced hysteretic behavior. To the best of our knowledge, this specific hybrid bifurcation mechanism—combining a local saddle-node annihilation with a transition to a remote attractor—has not been previously reported in photonic microcavities or similar dissipative systems. Related phenomena involving multistability and hidden attractors have been studied in other nonlinear systems [47,48], but not in the context of phase-controlled bistable transitions in integrated resonators. The presence of coexisting equilibrium points and long-lived SP states introduces a complex bifurcation landscape with both local and global features, which warrants further theoretical exploration. Crucially, this bifurcation does not conform to the characteristics of either a supercritical or subcritical Hopf bifurcation [19,49]. In conventional Hopf bifurcations, the onset of oscillations occurs when a pair of complex-conjugate eigenvalues crosses the imaginary axis [50]. In the presented results, however, two eigenvalues reduce to zero and annihilate, while the other two converge to a single real value and also annihilate (see Appendix B). Nor does the system behavior align with global bifurcations such as heteroclinic transitions, which involve orbits connecting saddle points [51]. Instead, the transition here is triggered by the annihilation of a saddle node and a stable fixed point, with the system abruptly jumping to a preexisting, distant attractor—specifically, a stable limit cycle that is not directly involved in the local bifurcation event.

C. Experimental dynamics near the saddle-node annihilation

After the bifurcation, the system must traverse the phase space to reach the attractor surrounding the unstable equilibrium, where stable SP sets in. Although the attractive node is annihilated, its former basin of attraction is not entirely eliminated. A remnant—often referred to as the *ghost* of the former attractor—persists and influences the system's dynamics, effectively slowing the system's evolution as it transitions to the new oscillatory state [52]. This ghost fades progressively as the phase shift introduced by PSL moves further from the bifurcation point. Beyond this region, the system settles into SP dynamics around the remaining unstable equilibrium.

To probe this transition, we measured the temporal response of the DRUM to a square-wave optical excitation with alternating *off* and *on* intervals of approximately 56 and 87 μs, respectively. This pulsed excitation ensures operation in a path-independent regime, as the DRUM returns to its rest state during each *off* period. The measurements were performed using the *modulated* experimental setup described in Appendix A. Figures 5(a)–5(c) show the transmission signal as a function of time at an average input power of approximately 3.8 mW. Figure 5(a) displays the response at $\phi_{12} = 0$ and large negative detuning, far from resonance. The response simply follows the square modulation. In contrast, Fig. 5(b) shows the time-domain response for small positive detuning at $\phi_{12} = 0.31\pi$, revealing a slow SP rise consistent with ghost-induced delay. An enlarged view of this response is shown in the left panel of Fig. 5(c), while the right panel of Fig. 5(c) shows the response at $\phi_{12} = 0.1\pi$, where the delay is even more pronounced. The corresponding wavelength detuning is indicated by the red dashed line in the transmission spectrum shown in the inset of Fig. 5(d).

The time traces in Fig. 5(c) highlight the onset time of SP, denoted by Δt and indicated with red arrows. Each trace exhibits a peak at the beginning of the *on* phase, followed by a dip and then a gradual rise in intensity leading to the onset of oscillations. For consistency, we define Δt as the time interval between this initial peak and the subsequent minimum. Notably, during this onset period, the system does not exhibit any oscillations. This is consistent with the theoretical prediction that the eigenvalues of the relevant equilibrium points remain strictly real [53] (see also Appendix B). The onset time Δt depends strongly on ϕ_{12}, as illustrated in Fig. 5(d), which plots Δt versus PSL phase during a reverse scan. Here, blue points correspond to stationary (nonoscillating) states, while black points indicate the presence of SP. Each Δt value represents the average of ten independent measurements; error bars denote the standard deviation. The traces shown in Fig. 5(c) correspond to the triangle and square markers on this graph. As expected, Δt increases nonlinearly as ϕ_{12} approaches the critical value at which saddle-node annihilation occurs. This trend is attributed to the growing influence of the ghost of the attractor, whose effective basin of attraction expands near the bifurcation [52]. Note that the ghost-delayed dynamics observed after a saddle-node annihilation are fundamentally distinct from a standard thermal delay, as they originate from the remnant of the basin of attraction associated with the annihilated stable node, which can in principle give rise to arbitrarily long settling times. Unlike thermal delays, which have a fixed timescale (of the order of 100 ns) the observed delay (up to approximately 50 μs) depends on control parameters, highlighting a complex interplay of effects beyond simple thermal relaxation.

D. Stable SP with a constant phase sum

The analysis of equilibrium points shows that the equilibrium remains unchanged provided that $\phi_{12} + \phi_{21}$ is held constant. This invariance arises because the equilibrium condition depends on the product of the complex coupling coefficients, $\beta_{12}\beta_{21} = |\beta_{12}||\beta_{21}|e^{i(\phi_{12}+\phi_{21})}$ [see Eq. (28) in Sec. S4 of the Supplemental Material [39]]. Consequently, a simultaneous variation of ϕ_{12} and ϕ_{21} that preserves their sum does not alter the system's equilibrium configuration or its spectral response. In the DRUM architecture, this condition can be experimentally implemented by jointly actuating both PSL and PSR in the side lobes. It is important to note that this condition differs fundamentally from the conventional Hermitian coupling condition, which requires $\beta_{12} = -\beta_{21}^*$ [54]. The Hermitian coupling condition ensures symmetric energy exchange between the counterpropagating modes, resulting in a balanced doublet in the optical transmission spectrum. In contrast, the constant-phase condition preserves the total intracavity energy during the sweep, allowing for a constant—though potentially asymmetric—energy exchange between the counterpropagating modes.

Figure 6 presents the measured SP frequency [Fig. 6(a)] and normalized average transmission [Fig. 6(c)], alongside the corresponding theoretical predictions [Figs. 6(b)

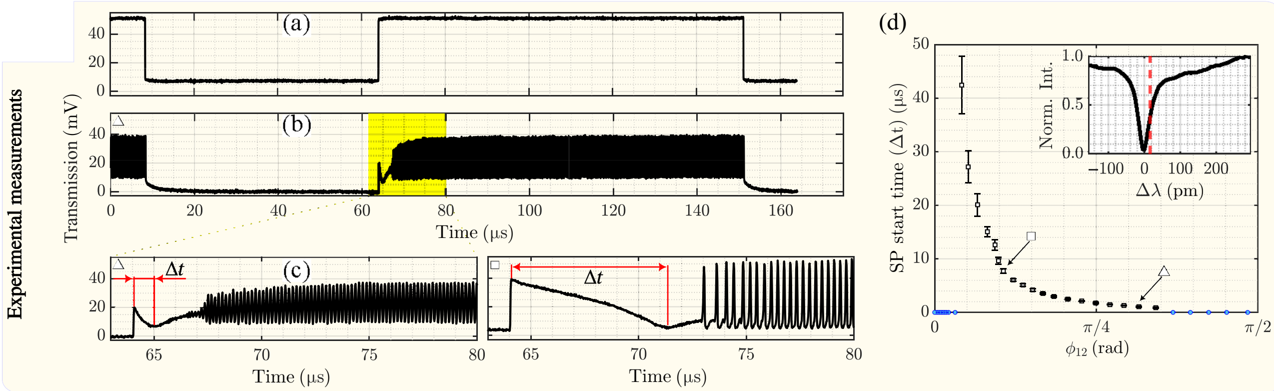

FIG. 5. Experimental evidence of the saddle-node ghost. (a) Transmission for a wavelength out of resonance as a function of time for a square input signal. Switching off the input signal allows the initial state to be reset, permitting measurements in the *path-independent phase* regime. (b) Transmission as a function of time at resonance for a wavelength detuning indicated by the red dashed line in the inset of (d), shown for the ϕ_{12} value marked by the triangle in (d), at about $\phi_{12} = 0.31\pi$. A dip in the *on* state is followed by the onset of SP. (c) Left: enlarged view of the initial time of the *on* state (yellow region) in (b). Right: start of the *on* state transmission for ϕ_{12} value marked by a square in (d), at approximately $\phi_{12} = 0.1\pi$. The red arrows define the SP onset time (Δt). (d) Plot of Δt as a function of ϕ_{12} for a reverse sweep. Squares in the SP regime, blue circles when no SP is observed. Inset: low-power resonance transmission at $\phi_{12} = 0$ (black lines); the red dashed line indicates the wavelength detuning used to measure the onset times.

and 6(d)], as functions of wavelength detuning and joint variations of ϕ_{12} and ϕ_{21}. In this configuration, ϕ_{12} is swept through a full-cycle reverse scan, while ϕ_{21} is varied through a full-cycle forward scan, such that their sum remains constant. During the measurement, the system operates in a path-dependent phase-rotation regime: for each detuning value $\Delta\lambda$, memory is preserved between successive phase configurations, while the system is reset to its initial state by switching off the input laser between different $\Delta\lambda$ values. For a fixed $\Delta\lambda$, both experiment and simulation show that the SP frequency remains nearly constant throughout the phase sweep, within the experimental uncertainties. This observation confirms that the system not only retains the same equilibrium condition but also follows an identical dynamical trajectory, consistent with the theoretical prediction that the equilibrium depends only on the sum $\phi_{12} + \phi_{21}$. Moreover, across all phase configurations, the SP frequency increases monotonically with wavelength detuning, as seen in both Figs. 6(a) and 6(b). The normalized average transmission [Fig. 6(c)] exhibits small fluctuations as a function of phases at fixed detuning, which are not observed in the theoretical map [Fig. 6(d)], where a flat response is predicted. These experimental deviations are attributed to minor uncertainties in the exact phase values achieved during the simultaneous variation of ϕ_{12} and ϕ_{21}. Overall, the excellent agreement between experimental and theoretical results reinforces the prediction from the stability analysis (see Secs. S4

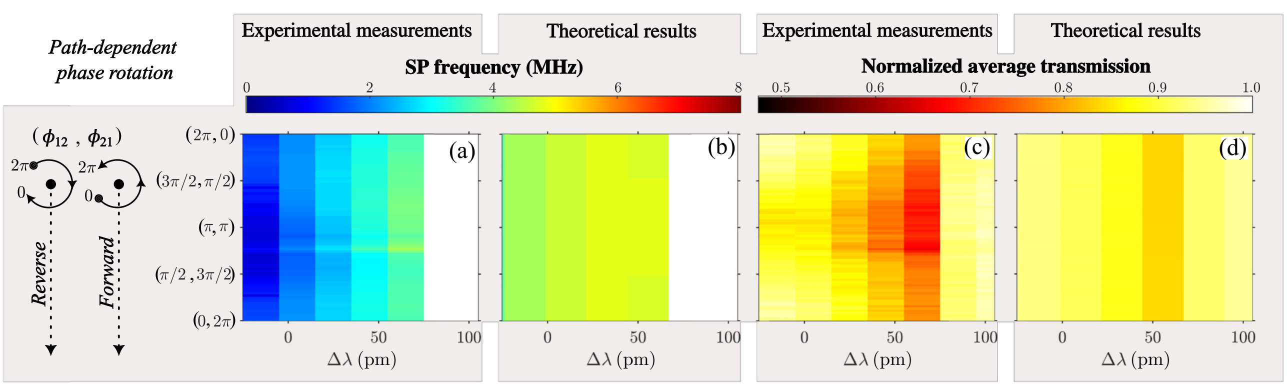

FIG. 6. Maps of SP frequency and normalized average transmission under full-cycle path-dependent phase rotation with fixed phase sum. (a),(c) Experimental SP frequency and normalized average transmission as a function of wavelength detuning ($\Delta\lambda$) and phases. The phases ϕ_{12} and ϕ_{21} are simultaneously varied in such a way that their sum is constant at $\phi_{12} + \phi_{21} = 2\pi$, i.e., current was injected in both PSL and PSR of the DRUM. Here, ϕ_{12} is swept from 2π to 0 (*reverse*), while ϕ_{21} is swept from 0 to 2π (*forward*). (b),(d) Theoretical simulations under the same conditions.

and S5 of the Supplemental Material [39]) that the system dynamics—both in terms of equilibrium structure and SP characteristics—are governed primarily by the internal cavity energy, which remains invariant when $\phi_{12} + \phi_{21}$ is held constant. These results confirm that, under the constant-phase-sum condition, not only is the equilibrium preserved, but the entire phase-space trajectory is effectively stabilized, allowing for robust and predictable dynamical behavior.

IV. CONCLUSION

We have experimentally explored the nonlinear dynamics of the dynamically reconfigurable unified microresonator (DRUM), a silicon microring system that enables controlled energy exchange between counterpropagating optical modes. By operating under non-Hermitian coupling conditions, we revealed how the nonlinear response evolves with phase tuning, showing strong agreement with theoretical predictions.

A central result is the emergence of path dependence: forward and reverse phase sweeps lead to different final states, even from identical initial conditions. This asymmetry reveals underlying bifurcation mechanisms that do not conform to standard Hopf bifurcations [49]. Instead, we observe nonlocal transitions in which the system jumps from a stable node to a distant limit cycle following a saddle-node annihilation. This behavior breaks the time-translation symmetry and generates hysteresis not typically seen in classical microring systems or conventional models of optical bistability [44,55]. Our study of the nonlinear response of the DRUM differs from previous investigations of integrated non-Hermitian photonic structures, which typically exhibit minimal or no tunability [36,37]. Moreover, previous efforts have primarily focused on chiral effects that lead to direction-dependent transmission and, consequently, to the breaking of Lorentz reciprocity [34,36,37,56]

Our analysis indicates that the DRUM undergoes a global bifurcation marked by a sudden change in the mean energy stored in the cavity and the onset of oscillations. Although the transition to oscillations is abrupt and could be reminiscent of a canard explosion [19,52], our system exhibits a saddle-node annihilation, where the disappearance of fixed points leaves behind a ghost structure that slows down the dynamics in the transitional stage. Experimental measurements of self-pulsing onset time as a function of phase confirm this interpretation. Although the observed transition shares qualitative features with several standard bifurcations, it is distinct from all of them. Unlike the saddle-node annihilation typical of FitzHugh-Nagumo-type models [57], where the initial and final states both reside either in stable fixed points or in limit cycles, our system undergoes the annihilation of a stable equilibrium followed by a forced migration toward a distant limit cycle. In contrast to both supercritical and subcritical Hopf bifurcations, the transition is not mediated by a change of stability of an equilibrium [50] but by the complete disappearance of the equilibrium itself. Finally, unlike a saddle-node-on-invariant-circle bifurcation [58], where oscillations emerge with arbitrarily low frequency due to prolonged residence near the ghost of the annihilated fixed point, our bifurcation does not exhibit a vanishing-frequency onset, indicating a fundamentally different dynamical mechanism. Moreover, by tuning both phases while preserving their sum, we maintain constant cavity energy and achieve phase-insensitive self-pulsing—highlighting coherent phase control as a robust tool for dynamical modulation.

These results position the DRUM as a reconfigurable platform for exploring rich dynamical phenomena, with implications beyond optics. The observed bifurcation dynamics bear resemblance to excitability in biological neurons, yet they differ from classical models such as FitzHugh-Nagumo and Hodgkin-Huxley, which exhibit local saddle-node-on-invariant-circle transitions [59,60]. Instead, the DRUM displays a saddle-node-annihilation-induced global switch of attractor. This suggests a previously unexplored neuromorphic regime that may also be relevant to biological excitable systems [23], and one that can now be studied in a scalable, silicon-integrated photonic platform. As such, the DRUM provides both a testbed for nonlinear science and a promising direction for neuromorphic photonics. In this context, the controlled hysteresis demonstrated in this work can be used as a short-term flip-flop memory [21] by generating two states with distinct mean values of the optical field. Controlling these states enables feedback mechanisms, allowing online training of the system. Furthermore, the two states exhibit different mean values, with self-pulsing dynamics superimposed on each. This behavior is uncommon in typical bistability phenomena observed in silicon microresonators and is potentially valuable for spiking neural networks. This work provides a proof-of-concept demonstration, with relatively slow phase variation due to the use of thermal phase shifters; however, this limitation can be overcome using faster refractive-index-modulation technologies, such as *p-i-n* junctions. From a broader perspective, the DRUM can be considered an artificial neuron, like a conventional silicon microresonator [40,61], but it offers the distinct advantage of controlling the energy stored in the cavity. This capability may enable tuning of key properties of biological neurons, including the firing threshold, refractory period, and integrate-and-fire temporal dynamics.

ACKNOWLEDGMENTS

We gratefully thank Dr. Iacopo Carusotto, Professor Leonardo Ricci and Professor Davide Bigoni for useful suggestions and interesting discussions. This project has received funding from the European Research Council (ERC) under the European Union's Horizon 2020 research and innovation programme (Grant Agreement No. 788793, BACKUP), from the MIUR under the PRIN PELM project (20177 PSCKT), and from the European Union under NextGenerationEU Project No. PRIN2022AEEKNC. S.B. acknowledges the cofinancing from European Union—Next Generation EU, Missione 4 Componente 2—CUP E53D23002230006.

S.B. conceived the idea of inducing controllable nonlinearity and memory using the DRUM. S.B., B.A., and R.F. conceived the experiment. R.F. designed the DRUM structure. B.A. and D.O. performed the measurements with the help of S.B. D.O. and S.B. analyzed the data with support from B.A. S.G. developed the theoretical model with the help of S.B. S.B. and S.G. wrote the manuscript with contributions from all coauthors. L.P. supervised the work. All authors discussed the results and contributed to the revision of the manuscript.

The authors declare no competing interests.

DATA AVAILABILITY

The data that support the findings of this article are not publicly available. The data are available from the authors upon reasonable request.

APPENDIX A: EXPERIMENTAL SETUP

The details of the DRUM silicon-on-insulator integrated device are described in Ref. [38]; however, it is worth stressing that, as reported in Sec. III A, the DRUM demonstrates high robustness against thermal crosstalk. This robustness is achieved by introducing 5-μm-wide trenches on both sides of each microheater, together with additional auxiliary trenches. The main trenches are positioned at a distance of 5 μm from the microheaters. These thermal-isolation barriers prevent heat propagation through the material and suppress global heating of the structure. The optical properties of the DRUM are measured using the setup shown schematically in Fig. 7. A fiber-based continuous-wave tunable laser (CWTL, Yenista Optics, TUNICS-T100S) operating in the C-band is amplified by an erbium-doped fiber amplifier (EDFA, IPG Photonics) and sent to a fiber switch (FS). The switch selects between two types of excitation: *constant* or *modulated*. In the *constant* mode, the signal is directly attenuated by an electronic variable optical attenuator (VOA in). In the *modulated* mode, the signal first passes through an electro-optic modulator (EOM, iXblue, MXAN-LN-10), driven by an arbitrary-waveform generator (AWG, Teledyne, T3AFG500) and is then attenuated by VOA in. The polarization of the optical signal is then adjusted using a polarization controller (PC), and a 10% tap is used to monitor the average input power via a photodetector (PD, 30 kHz). The remaining 90% of the signal is directed into an optical circulator (OC), which routes it to the input of the device via a stripped fiber mounted on a three-axis piezoelectric stage for precise alignment. At the output grating coupler of the DRUM, another stripped fiber, also mounted on a three-axis piezoelectric stage, collects the optical response. The output signal passes through another OC and a second variable optical attenuator (VOA out) before being detected by a PD (1.2 GHz). The input OC enables reflection measurements of the DRUM using an additional PD (1.2 GHz), while the output OC suppresses spurious reflections. The electrical signals from the PDs are acquired by an oscilloscope (LeCroy WavePro 7300 A, 3 GHz) and stored on a computer that also controls the various components in the setup (as indicated by the black arrows in Fig. 7). The current applied to the PSs is controlled via a write breadboard (WB, NI CompactDAQ), and the optical chip is mounted on a thermostat holder whose temperature

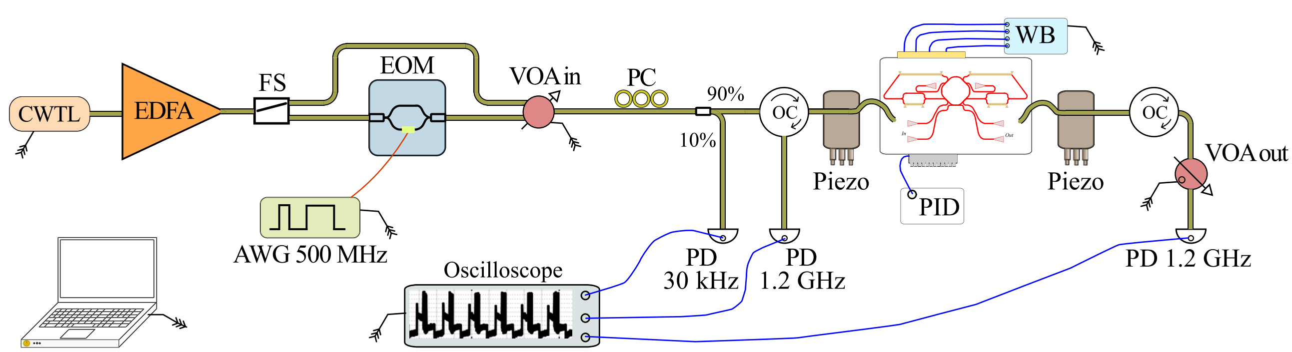

FIG. 7. Schematic diagram of the experimental setup. A fiber-optic switch (FS) allows selection between two operating modes: *constant* and *modulated*. In the *constant* mode, the amplified signal is injected directly into the input port of the DRUM. In the *modulated* mode, the signal is modulated by an electro-optic modulator (EOM) before being sent to the input port. The response of the DRUM is detected by a photodetector (PD) and recorded using an oscilloscope. All symbols are defined in the text.

TABLE I. Eigenvalues of the Jacobian associated with free carriers and temperature for different values of phase ϕ_{12} and for different equilibria. The numbers allow the eigenvalues to be related to the points shown in Fig. 4.

(a)			(b)			(c)		
I			**II**			**III**		
$\phi_{12} = 0$	$\widetilde{\lambda}_1$	$\widetilde{\lambda}_2$	$\phi_{12} = 0.37\pi$	$\widetilde{\lambda}_1$	$\widetilde{\lambda}_2$	$\phi_{12} = 0.75\pi$	$\widetilde{\lambda}_1$	$\widetilde{\lambda}_2$
rad	MHz	MHz	rad	MHz	MHz	rad	MHz	MHz
#1	−100.3	−9.6	#2$^-$	−230.6	−0.006	…	…	…
#3	−583.2	11.6	#2$^+$	−250.6	0.9	…	…	…
#6	29.0	613.7	#5	24.1	666.4	#4	27.2	315.5

is controlled by a proportional-integral-derivative (PID, SIM960) controller connected to a Peltier cell and a 10 kΩ thermistor.

APPENDIX B: EIGENVALUES AT THE EQUILIBRIUM POINTS

Table I presents the values of the eigenvalues evaluated at the equilibrium points depicted in Fig. 4, based on the analytical framework described in Sec. S5 of the Supplemental Material [39].

It is important to note that all eigenvalues associated with the equilibrium points are real. As a consequence, no oscillatory behavior is expected when the system evolves near these equilibria, since purely real eigenvalues preclude spiral trajectories in phase space [53]. This is consistent with the experimental observation of a nonoscillatory onset phase in Fig. 5, where the system lingers near the ghost of the former attractor before entering the SP regime. The structure of the eigenvalue spectrum, summarized in Table I, provides further insight into the dynamics. At $\phi_{12} = 0$ (line I), we identify a stable equilibrium (point #1, with both eigenvalues negative), a saddle point (point #3, with eigenvalues of opposite sign), and a fully unstable equilibrium (point #6, with both eigenvalues positive). As illustrated in Fig. 4(h), an attractive limit cycle surrounds the fully unstable point, serving as the destination of the system once the stable node is lost. As the phase increases to $\phi_{12} = 0.37\pi$ (line II), just prior to the saddle-node annihilation, the eigenvalues associated with points #1 and #3 begin to converge. Although point #2 appears as a distinct equilibrium in Fig. 4, the proximity of #1 and #3 at this phase suggests their imminent coalescence. This motivates the notation #2$^-$ (approaching from the stable side) and #2$^+$ (approaching from the saddle). Notably, the first eigenvalue—negative and associated with the saddle—approaches a value near −240 MHz, while the second eigenvalues of both points tend toward zero. We interpret this behavior as indicative of the vanishing repulsive component of the saddle. After the annihilation, the remnant ghost inherits a purely attractive character, which is consistent with the absence of any transient repulsion during the onset of SP in Fig. 5. Throughout the phase evolution—specifically at $\phi_{12} = 0, 0.37\pi$, and 0.75π—the eigenvalues corresponding to points #6, #5, and #4 remain strictly positive, confirming that these equilibria persist as fully unstable nodes throughout. This spectral configuration supports the interpretation of the bifurcation as a global saddle-node-annihilation-induced switch of attractor.

[1] R. El-Ganainy, K. G. Makris, M. Khajavikhan, Z. H. Musslimani, S. Rotter, and D. N. Christodoulides, Non-Hermitian physics and PT symmetry, Nat. Phys. **14**, 11 (2018).

[2] Ş. K. Özdemir, S. Rotter, F. Nori, and L. Yang, Parity–time symmetry and exceptional points in photonics, Nat. Mater. **18**, 783 (2019).

[3] K. Sone, K. Yokomizo, K. Kawaguchi, and Y. Ashida, Hermitian and non-Hermitian topology in active matter, Rep. Prog. Phys. **89**, 016501 (2026).

[4] Y. Ashida, Z. Gong, and M. Ueda, Non-Hermitian physics, Adv. Phys. **69**, 249 (2020).

[5] M. V. Berry, Physics of nonhermitian degeneracies, Czech. J. Phys. **54**, 1039 (2004).

[6] M.-A. Miri and A. Alù, Exceptional points in optics and photonics, Science **363**, eaar7709 (2019).

[7] A. Calabrese, F. Ramiro-Manzano, H. M. Price, S. Biasi, M. Bernard, M. Ghulinyan, I. Carusotto, and L. Pavesi, Unidirectional reflection from an integrated "Taiji" microresonator, Photonics Res. **8**, 1333 (2020).

[8] L. Feng, X. Zhu, S. Yang, H. Zhu, P. Zhang, X. Yin, Y. Wang, and X. Zhang, Demonstration of a large-scale optical exceptional point structure, Opt. Express **22**, 1760 (2014).

[9] Y. Chen, J. Li, K. Xu, S. Biasi, R. Franchi, C. Huang, J. Duan, X. Wang, L. Pavesi, X. Xu, *et al.*, Electrically reconfigurable mode chirality in integrated microring resonators, Laser Photonics Rev. **18**, 2301289 (2024).

[10] S. Soleymani, Q. Zhong, M. Mokim, S. Rotter, R. El-Ganainy, and Ş. Özdemir, Chiral and degenerate perfect absorption on exceptional surfaces, Nat. Commun. **13**, 599 (2022).

[11] H. Lee, A. Kecebas, F. Wang, L. Chang, S. K. Özdemir, and T. Gu, Chiral exceptional point and coherent suppression

of backscattering in silicon microring with low loss Mie scatterer, Elight **3**, 20 (2023).

[12] C. Wang, W. R. Sweeney, A. D. Stone, and L. Yang, Coherent perfect absorption at an exceptional point, Science **373**, 1261 (2021).

[13] H. Hörner, L. Wild, Y. Slobodkin, G. Weinberg, O. Katz, and S. Rotter, Coherent perfect absorption of arbitrary wavefronts at an exceptional point, Phys. Rev. Lett. **133**, 173801 (2024).

[14] J. Wiersig, Review of exceptional point-based sensors, Photonics Res. **8**, 1457 (2020).

[15] J. Lyu, Z. Gao, L. Feng, and L. Ge, Non-Hermitian gauged reciprocity and symmetry, Phys. Rev. B **110**, 134102 (2024).

[16] H. Hodaei, M.-A. Miri, M. Heinrich, D. N. Christodoulides, and M. Khajavikhan, Parity-time–symmetric microring lasers, Science **346**, 975 (2014).

[17] X. Z. Hao, X. Y. Zhang, Y. H. Zhou, W. Li, S. C. Hou, and X. X. Yi, Gain-saturation-induced self-sustained oscillations in non-Hermitian optomechanics, Phys. Rev. A **103**, 053508 (2021).

[18] E. M. Izhikevich, *Dynamical Systems in Neuroscience: The Geometry of Excitability and Bursting* (The MIT Press, Cambridge, MA, 2007).

[19] S. H. Strogatz, *Nonlinear Dynamics and Chaos: With Applications to Physics, Biology, Chemistry, and Engineering* (CRC Press, Boca Raton, FL, 2024).

[20] A. L. Hodgkin and A. F. Huxley, A quantitative description of membrane current and its application to conduction and excitation in nerve, J. Physiol. **117**, 500 (1952).

[21] G. Donati, D. Owen-Newns, J. Robertson, E. Malysheva, A. Adair, J. Figueiredo, B. Romeira, V. Dolores-Calzadilla, and A. Hurtado, Spiking flip-flop memory in resonant tunneling diode neurons, Phys. Rev. Lett. **133**, 267301 (2024).

[22] S. Yu, X. Piao, and N. Park, Neuromorphic functions of light in parity-time-symmetric systems, Adv. Sci. **6**, 1900771 (2019).

[23] S. Biasi, A. Foradori, R. Franchi, A. Lugnan, P. Bienstman, and L. Pavesi, The Taiji microresonator as an unidirectional spiking neuron, ArXiv:2410.03257.

[24] K. Sriram, Effects of positive electrical feedback in the oscillating Belousov–Zhabotinsky reaction: Experiments and simulations, Chaos Solitons Fract. **28**, 1055 (2006).

[25] J. E. Marsden and M. McCracken, *The Hopf Bifurcation and its Applications* (Springer-Verlag, New York, NY, 2012).

[26] C. Masoller, Coherence resonance in delayed feedback systems, Phys. Rev. Lett. **86**, 2782 (2001).

[27] P. Jung and G. Mayer-Kress, Delay-induced oscillations in nonlinear systems, Phys. Lett. A **261**, 386 (2001).

[28] S. Barbay, R. Kuszelewicz, and A. J. Yacomotti, Excitable laser with optical injection: Temporal response and triggering thresholds, Opt. Lett. **36**, 4476 (2011).

[29] R. Faggiani and P. Lalanne, Non-Markovian dynamics in photonic crystal cavities, Sci. Rep. **6**, 27037 (2016).

[30] H.-P. Breuer, E.-M. Laine, J. Piilo, and B. Vacchini, Colloquium: Non-Markovian dynamics in open quantum systems, Rev. Mod. Phys. **88**, 021002 (2016).

[31] J. Leuthold, C. Koos, and W. Freude, Nonlinear silicon photonics, Nat. Photonics **4**, 535 (2010).

[32] D. A. Miller, Silicon photonics: Meshing optics with applications, Nat. Photonics **11**, 403 (2017).

[33] M. Borghi, C. Castellan, S. Signorini, A. Trenti, and L. Pavesi, Nonlinear silicon photonics, J. Opt. **19**, 093002 (2017).

[34] J. Qie, C. Wang, and L. Yang, Chirality induced nonreciprocity in a nonlinear optical microresonator, Laser Photonics Rev. **17**, 2200717 (2023).

[35] J. Li, K. Li, W. Li, J. Wang, Y. Yao, Y. Sun, Y. Zou, J. Wang, F. He, J. Duan, *et al.*, Low-threshold chirality-enabled silicon photonic diode, Laser Photonics Rev. **19**, e02078 (2025).

[36] A. Muñoz de las Heras, R. Franchi, S. Biasi, M. Ghulinyan, L. Pavesi, and I. Carusotto, Nonlinearity-induced reciprocity breaking in a single nonmagnetic Taiji resonator, Phys. Rev. Appl. **15**, 054044 (2021).

[37] H. Lee, L. Chang, A. Kecebas, D. Mao, Y. Xiao, T. Li, A. Alù, S. K. Özdemir, and T. Gu, Chiral exceptional point enhanced active tuning and nonreciprocity in microresonators, Light: Sci. Appl. **14**, 45 (2025).

[38] B. Aslan, R. Franchi, S. Biasi, S. Ali, D. Olivieri, and L. Pavesi, Coherent control of (non-)Hermitian mode coupling: Tunable chirality and exceptional point dynamics in photonic microresonators, Light: Sci. Appl. (2025). (to be published).

[39] See Supplemental Material at http://link.aps.org/supplemental/10.1103/fcsp-jw79 for the analytical linear response of the DRUM, the nonlinear governing equations, the procedure used to remove path-dependent phase effects by laser on-off switching between consecutive measurements, the equilibrium-point analysis, and the method used to evaluate the eigenvalues. The Supplemental Material also contains Refs. [62,63].

[40] T. Van Vaerenbergh, M. Fiers, P. Mechet, T. Spuesens, R. Kumar, G. Morthier, B. Schrauwen, J. Dambre, and P. Bienstman, Cascadable excitability in microrings, Opt. Express **20**, 20292 (2012).

[41] S. Biasi, R. Franchi, D. Bazzanella, and L. Pavesi, On the effect of the thermal cross-talk in a photonic feed-forward neural network based on silicon microresonators, Front. Phys. **10**, 1093191 (2022).

[42] T. Van Vaerenbergh, M. Fiers, J. Dambre, and P. Bienstman, Simplified description of self-pulsation and excitability by thermal and free-carrier effects in semiconductor microcavities, Phys. Rev. A **86**, 063808 (2012).

[43] M. Borghi, D. Bazzanella, M. Mancinelli, and L. Pavesi, On the modeling of thermal and free carrier nonlinearities in silicon-on-insulator microring resonators, Opt. Express **29**, 4363 (2021).

[44] G. Priem, P. Dumon, W. Bogaerts, D. Van Thourhout, G. Morthier, and R. Baets, Optical bistability and pulsating behaviour in silicon-on-insulator ring resonator structures, Opt. Express **13**, 9623 (2005).

[45] L. Pavesi, Thirty years in silicon photonics: A personal view, Front. Phys. **9**, 786028 (2021).

[46] M. R. Guevara, in *Nonlinear Dynamics in Physiology and Medicine* (Springer, New York, NY, 2003), p. 41.

[47] G. A. Leonov and N. V. Kuznetsov, Hidden attractors in dynamical systems: From hidden oscillations in Hilbert–Kolmogorov, Aizerman, and Kalman problems to hidden chaotic attractors in Chua circuits, Int. J. Bifurc. Chaos **23**, 1330002 (2013).

[48] M. Cencini, F. Cecconi, and A. Vulpiani, *Chaos: From Simple Models to Complex Systems* (World Scientific, Singapore, 2010).

[49] D. H. Rothman, *Nonlinear Dynamics: Chaos* (Massachusetts Institute of Technology: MIT OpenCourseWare, Cambridge, MA, 2022).

[50] Y. A. Kuznetsov, *Elements of Applied Bifurcation Theory*, 3rd ed.Applied Mathematical Sciences (112, Springer, 2013), Vol.

[51] J. Guckenheimer and P. Holmes, *Nonlinear Oscillations, Dynamical Systems, and Bifurcations of Vector Fields*, Applied Mathematical Sciences (42.Springer, 1983), Vol.

[52] S. H. Strogatz and R. M. Westervelt, Predicted power laws for delayed switching of charge-density waves, Phys. Rev. B **40**, 10501 (1989).

[53] S. Gretter, M. Mancinelli, and L. Pavesi, Dynamic analysis and reservoir computing application of a nonlinear microring resonator, ACS Photonics **12**, 4956 (2025).

[54] S. Biasi, F. Ramiro-Manzano, F. Turri, P.-É. Larré, M. Ghulinyan, I. Carusotto, and L. Pavesi, Hermitian and non-Hermitian mode coupling in a microdisk resonator due to stochastic surface roughness scattering, IEEE Photonics J. **11**, 1 (2018).

[55] V. R. Almeida and M. Lipson, Optical bistability on a silicon chip, Opt. Lett. **29**, 2387 (2004).

[56] R. Franchi, S. Biasi, A. M. de Las Heras, M. Ghulinyan, I. Carusotto, and L. Pavesi, Influence of the bus waveguide on the linear and nonlinear response of a Taiji microresonator, Opt. Express **29**, 29615 (2021).

[57] Z. Jing, Y. Chang, and B. Guo, Bifurcation and chaos in discrete Fitzhugh–Nagumo system, Chaos Solitons Fract. **21**, 701 (2004).

[58] I. Al-Darabsah and S. A. Campbell, M-current induced Bogdanov–Takens bifurcation and switching of neuron excitability class, J. Math. Neurosci. **11**, 1 (2021).

[59] W. E. Sherwood, in *Encyclopedia of Computational Neuroscience* (Springer, New York, NY, 2015), p. 1202.

[60] Z. Zhao and H. Gu, Transitions between classes of neuronal excitability and bifurcations induced by autapse, Sci. Rep. **7**, 6760 (2017).

[61] J. Xiang, A. Torchy, X. Guo, and Y. Su, All-optical spiking neuron based on passive microresonator, J. Lightwave Technol. **38**, 4019 (2020).

[62] S. Biasi, P. Guillemé, A. Volpini, G. Fontana, and L. Pavesi, Time response of a microring resonator to a rectangular pulse in different coupling regimes, J. Lightwave Technol. **37**, 5091 (2019).

[63] T. J. Johnson, M. Borselli, and O. Painter, Self-induced optical modulation of the transmission through a high-*Q* silicon microdisk resonator, Opt. Express **14**, 817 (2006).